Interfacial Electron Scattering in Nanocomposite Materials: Electrical Measurements to Reveal The Nc-MeN/a-SiN$_x$ Nanostructure in Order to Tune Macroscopic Properties

R. Sanjinés and C. S. Sandu

Additional information is available at the end of the chapter

http://dx.doi.org/10.5772/51123

1. Introduction

The impressive number of outstanding physical, chemical and mechanical properties of transition metal nitrides MeN (Me stands for transition metal Ti, V, Cr, Zr, Mo, Nb, Ta,..) makes then very attractive materials for many industrial applications as protective and decorative coatings [1,2], superconducting nanostructured thin films for single photon detectors [3,4], diffusion barriers in microelectronic devices [5,6], catalytic films [7,8], and also as materials for biomedical applications [9,10]. Depending on the oxidation states of the transition metal, the Me-N system can exhibit a rich variety of stable or metastable crystallographic phases. Thus, the tetragonal Me_2N and the cubic fcc structures are preferred for IVB-VA compounds (TiN, VN, ZrN) while for VB and VIB-VA compounds the stable phase is the hexagonal one (NbN, MoN, TaN and WN). In particular, as thin films MeN can be easily integrated in microelectronic devices and commonly used as diffusion barriers in magneto-resistive random access memory, resistors, excellent barrier diffusion against Cu, or as preferred barrier absorber material for EUV mask [4-8].

To further improve the performances and efficiency of MeN functional properties, nanocrystalline or amorphous ternary systems, such as Me-Al-N, Me-Si-N, and other Me-X-N forming highly stable compounds have been also investigated [11-30]. By addition of Al or Si to binary MeN, hardness, thermal stability and chemical inertness of the films can be improved [11-16]. In particular TiSiN, TaSiN, NbSiN and WSiN thin films have been mainly investigated as diffusion barriers and electrodes for phase change random access memory (PRAM) devices. [21-30]. The addition of Si leads to the formation of a nanocomposite

INTECH
open science | open minds

(nanocrystallites of MeN + amourphous SiN_x) or a solid solution single phase $Me_{1-x}Si_xN$ material [13-16]. In nanocomposite thin films (nc-MeN/a-SiN_x), crystallite sizes are of the order of few nanometers. The density of point defects (vacancies, interstitials, antisites), the grain size, the grain surfaces, and boundary regions play an increased role on physical properties. The arrangement and the chemical composition of the so-called “amorphous” minority phase (SiN_x) are crucial for electrical and mechanical properties [17-20]. The location, composition and the thickness of the amorphous phase must therefore be known precisely.

Usually these films are deposited by CVD [12, 15] or PVD [11, 14, 16] techniques; among the PVD techniques, magnetron reactive sputtering is often used as a low-temperature film growth technique. The macroscopic properties of these films such as mechanical, optical or electrical strongly depend on chemical composition and nanostructure of the resulting films which are influenced by the deposition parameters such as the substrate temperature, the flux and kinetic energy of impinging atomic and ionic species on the surface of the growing film, and the condensation rate.

The aim of this paper is to give a general overview on the relationship between the electrical and structural properties of binary MeN and nanocomposite nc-MeN/a-SiN_x thin films deposited by reactive magnetron sputtering. In particular we will focus on the possibility to use electrical measurements and electron scattering models to obtain pertinent information concerning the chemical composition, thickness and continuity of the insulating layer covering conducting nanocrystallites in nanocomposite films. It is not the purpose of this paper to develop further the models describing film nanostructure. This has already been extensively covered in much of the cited literature. The limitations of characterization techniques, such as HRTEM, XRD and XPS, in revealing such composite nanostructures, as described by various physical models, motivate us to employ unconventional investigation techniques such as electrical measurements in order to evidence, for example, the continuity of the insulating SiN_x-layer on conducting MeN-crystallites. The case of a special type of nanocomposite materials: nanocrystallites of Phase1 surrounded by a very thin interfacial layer of Phase2, obtained as a result of self-segregation is one of the most difficult to investigate. Instead, the goal of this paper is to discuss the ability of electrical measurements to support such models.

2. Film morphology and nanostructure

Depending on the deposition conditions binary transition metal nitride MeN thin films deposited by reactive magnetron sputtering usually crystallize with strong (111) or (200) preferential orientation and exhibit elongated crystallites in the grow direction [16-20,31] as one can notice from XRD or SEM measurements (Fig. 1). In MeXN (X=Si,Ge,B,Cu..), the addition of X leads to important modification of the films morphology. Thus, as a function of increasing X content (C_X), the average crystallite size, d, in many systems such as Ti-Si-N, Ti-Ge-N, Ti-Sn-N, Nb-Si-N, Zr-Si-N, Ta-Si-N, decreases from tens on nm to about 2 nm [16-20, 32-35]. Whether a ternary single-phase or composite multiphased system is formed depends on the chemical reactivity of the involved atoms and on the deposition conditions. In many case X atoms can substitute metal atoms in the fcc MeN lattice up to a critical concentration (limit of solubility, α_X). The segregation of X atoms on the MeN crystallite surface is mainly responsible for the limitation of their growth. It results in the formation of a nanocomposite material composed of a thin amorphous phase on the MeN crystallite surfaces. Frequently a relationship$d \propto 1/C_X$ is observed in MeXN films (see Fig. 2) suggesting that in this regime the increase in the X content determines a simultaneous increase in the surface-to-volume ratio of the MeN crystallites, which is realized by a subsequent decrease in the average crystallite sizes.

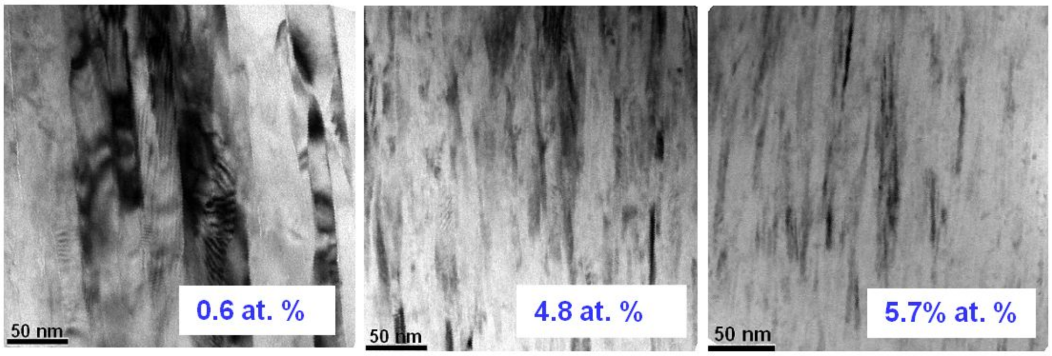

Figure 1. TEM images showing the evolution of the Zr-Si-N films morphology with increasing Si content.

3. Model for the Me-X-N film formation

The sketch given in Fig. 3 illustrates the growth model for the formation of Me-X-N ternary system. As a function of the X content, three X concentration regions can be identified. In the case of PVD deposition techniques such as magnetron sputtering, the film growth is frequently made out of thermodynamical equilibrium. Consequently the addition of X atoms in small quantities into the MeN lattice presents the introduction of structural points defects (substitutions, interstitials, vacancies), which might perturb the crystallite growth. This region 1 is called *Region* 1 or the region of pseudo-solubility of X atoms in MeN. The limit of the pseudo-solubility α_X of X depends on deposition conditions (substrate temperature and bias). Once the X content exceeds α_X the additional X atoms increasingly segregate and accumulate at the grain boundary regions. This concentration region is denoted as *Region* 2, in this region the surface of each X crystallite is progressively coated by a growing XN_y tissue layer up to a certain limit, referred to as the so-called X coverage level, X_{cov}. When X_{cov} =1 (full coverage), further increase of the X content leads to the formation of ultrathin XN_y layer surrounding completely the surface of the MeN crystallite and hindering the crystallite growth. Thus, in the *Region* 3 the, microstructure is strongly altered as a consequence of X segregation.

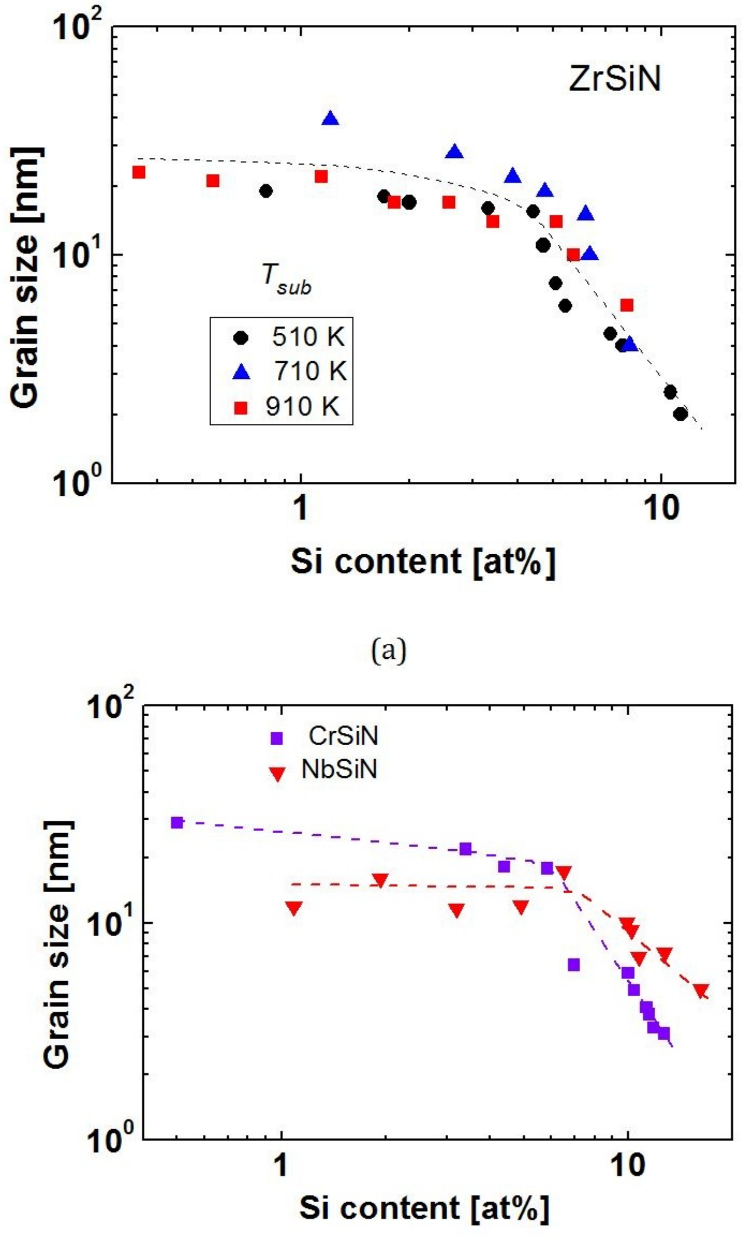

(a)

(b)

Figure 2. (a)Grain size vs. Si content in Zr-Si-N films. (b) Grain size vs. Si content in Cr-Si-N and Nb-Si-N thin films.

The degree of X surface-coverage of a crystallite of a typical size d can be determined in terms of C_X and C_{Me} concentrations considering a simple model. In a cubic shaped crystallite of volume $V_C = d^3$. For a fcc-NaCl-type structure each unit cell of volume a^3 contain 4 atoms, then the density of Me atoms in V_C is given by $N_{Me/Vc} = (4/a^3)d^3$ while its surface density is $N_{Me/Surf} = (2/a^2)(6d^2)$ (a is the lattice constant). The relation between the number of Me surface atoms and that of the volume is $N_{Me/Surf}/N_{Me/Vc} = (3\ a/d)$. Under the assumption that the segregated X atoms occupy the surface Me sites, the degree of the X coverage (X_{cov}) in terms of C_X and C_{Me} atomic per cent is then given by

$$X_{cov}=\left(\frac{N_{X/Surf}}{N_{Me/Surf}}\right)=\frac{N_{X/Surf}}{N_{Me/Vc}\left(3\frac{a}{d}\right)}=\frac{(C_X-\alpha_L)}{(C_{Me}+\alpha_L)\left(3\frac{a}{d}\right)} \tag{1}$$

In equation (1) the quantity α_L is the limit X solubility and takes into account of the amount of X atoms that are incorporated in the MeN:Si crystal lattice. As state above, in Me-X-N system the films generally exhibit a pronounced needle-like, columnar structure, with elongated crystallites where the length to width ratio higher than L/d=10 is observed. For such a situation, the relation (1) can be easily modified by introducing the vertical grain extension *L* as an integer multiple of the in plane crystallite dimension *L*=n*d*, note that in case of cubic-shaped crystallites n=1. Therefore the Si coverage for elongated crystallite is

$$X_{cov}=\frac{(C_X-\alpha_L)}{(C_{Me}+\alpha_L)\left(2+\frac{1}{n}\right)\left(\frac{a}{d}\right)} \tag{2}$$

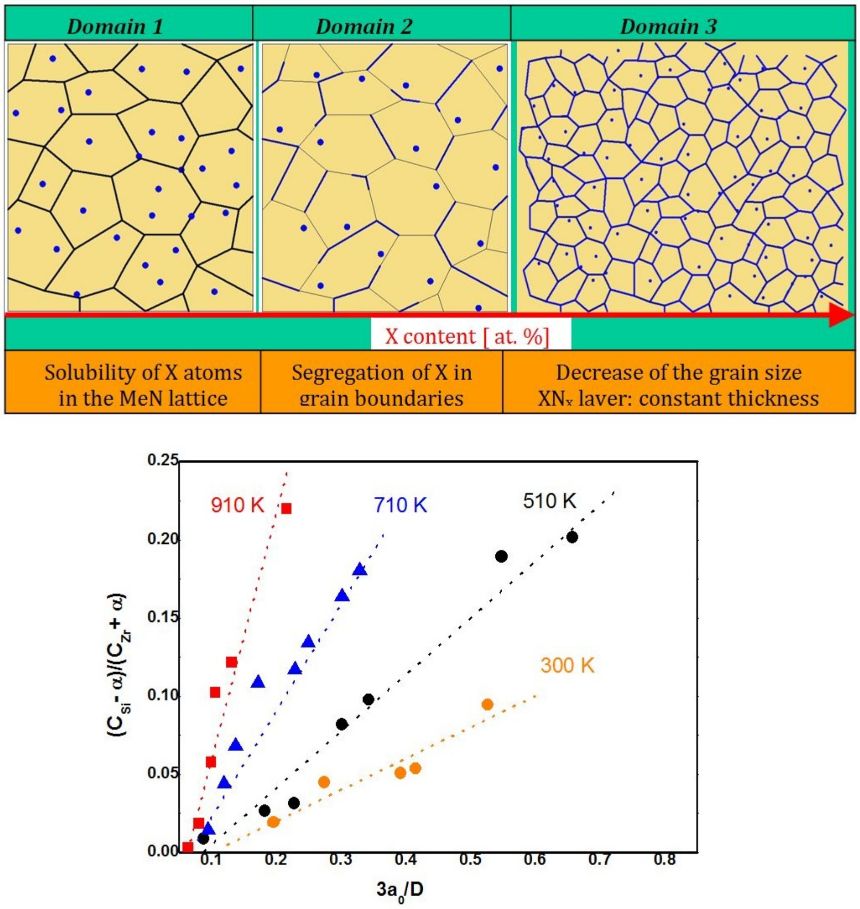

Figure 3. (a) Physical model describing the evolution of nanostructure with increasing X element content. (b) Correlation between secondary phase segregation at the grain boundaries and nanostructure in Zr-Si-N films deposited at various temperatures.

Interestingly, the relation (1,2) predicts that if X_{cov} remains constant, the average crystallite size d and the X content follow a linear relationship $C_X \approx cte \times \frac{1}{d}$, which is observed in many Me-X-N systems. Fig. 3b for example illustrates that the dependence of $\frac{(C_X - \alpha_L)}{(C_{Me} + \alpha_L)}$ on $\frac{3a}{d}$ for the ZrSiN films is linear and that X_{cov} can be evaluated from the slope of the curve.

4. Electrical properties

The electrical resistivity is strongly dependent on the film nanostructure. Not only the type of polycrystalline major phase and grain boundary phase (metal-like conductor, semiconductor or insulator), but also the grain size of crystalline phase, the thickness of grain boundary phase and the global film density are the main parameters that influence the resistivity of nanocomposite thin films. The thicknesses of the minority grain boundary phase (such as SiN_x, a-C, BN, or $TiGe_y$) can be calculated using the model for the film formation described in the section 3. Due to the fact that the charge carrier scattering is very sensitive to grain size and nature of the grain boundary regions, it should more convenient to plot the d.c. electrical resistivity values as a function of the grain size rather than to consider the atomic concentration C_X of the minority phase.

In the results presented in this section, the reported grain size values were obtained from XRD measurements, most of which were acquired in grazing incidence configuration. This value represents the mean value of the crystallite size in an oblique direction at about 15°-30° with respect to the film normal, the grain size values obtained from grazing incidence XRD are much closer to the lateral size of the crystallites. So, to a first approximation, these values could be considered as more suitable for calculating electrical parameters, due to the fact that the electrical resistivity is measured in the plane of the film. Obviously, some adjustment could be made in order to take into account the real lateral size of the crystallites, which can be obtained from TEM in cross-section.

4.1. Nanostructure and RT d.c. electrical resistivity

Depending on the atomic concentration of the minority phase and on the chemical composition of the main crystalline phase, the room temperature (RT) resistivity of MeXN nanocomposites can change over two or more orders of magnitude. It is worth noting that rather to plot the RT resistivity as a function of the atomic concentration of the minority phase it is more instructive to represent the RT resistivity as a function of the grain size in order to extricate the contribution of the structural film modification on the carriers transport properties. In this section, we will consider the nature of composites, how they can be classified from their dc electrical resistivity behavior, how these reflect the electrical properties of the constituent materials, and, in the next section, to what extent they can be modelled. Depending on the electrical nature of the polycrystalline mayor phase (metal-like conductor or semiconductor) and grain boundary tissue phase (conductor or isolator) three types of nanocomposites will be discussed: metal-like conductor/insulator (M-I), metal-like conductor/conductor (M-M), and semiconductor/insulator (S-I).

4.1.1. Metal-like conductor/Insulator (M-I) interfaces

The room temperature electrical resistivity of Zr-Si-N films, deposited at various temperatures and bias voltages are shown in Fig. 4a [19]. The influence of the crystallite size on the resistivity is clearly observed in the case of films deposited without bias at 510, 710 and 910 K. These films present a nanocomposite structure nc-ZrN/a-SiN$_x$. The formation of an amorphous SiN$_x$ insulating (a-SiN$_x$) layer on the ZrN nanocrystallite (nc-ZN) surface is responsible for significant increases in resistivity only for the films with silicon coverage Si_{cov} greater than 0.5 ML. It should be mentioned that 0.5 ML coverage layer corresponds to 1 ML of SiN$_x$ between two adjacent ZrN crystallites. Wherever such SiN$_x$ layers (thicker than 1.0 ML) are formed, it is observed a significant gap between the resistivity values at the same crystallite size value but at different values for SiN$_x$ thickness. The effect of grain boundary scattering on film resistivity is enhanced as grain size is decreased. This corresponds to the increase of the gap between the resistivity values of films deposited at 510 K, 710 K and 910 K with crystallite size reduction. Thus, the grain boundary scattering is enhanced in the case of the films showing higher SiN$_x$ surface coverage. The increase in resistivity with increasing Si content related to the formation of nanocomposite material showing an insulating and continuum layer between conducting nanocrystallites, has been reported in Zr-Si-N (nc-ZrN/SiN$_x$) [14], Nb-Si-N (nc-NbN/SiN$_x$) [18], Ta-Si-N (nc-TaSiN/SiN$_x$) [36] and Ti-B-N films (nc-TiB/BN) [37].

4.1.2. Conductor/Conductor (M-M) interfaces

In the case of M-M nanocomposites, the presence of a different conducting phase at the grain boundaries of conducting crystallites, does not strongly affect the resistivity behavior. Small changes in the densification, chemical composition of the films and high density of point defects at the grain boundary regions could induce the observed variations. In nitrogen-deficient or nitrogen-rich binary MeN$_{1\pm x}$ thin films, the resistivity can strongly depend on the chemical composition. Thus, in ZrN$_{1\pm x}$ and TaN$_{1\pm x}$ large variations of the resistivity (one to two orders of magnitude) as a function of the N content are observed. The N-deficiency also affects the electrical properties of Me-Si-N nanocomposites. For example, in the case of N-deficient (ZrSi)$_y$N$_x$ (with $x \leq 0.5$) films deposited at RT without bias, or at 300 K and 510 K with -150 V bias, it is observed that the resistivity does not change significantly with decreasing grain size (increasing Si content) as shown in Fig. 4a. The Si compositional independent behavior of the resistivity is supposed to be originated from direct percolation of the conducting ZrN$_{1-x}$ crystallites and/or ZrN$_{1-x}$ crystallites separated by low degree of nitridation of the SiN$_x$ grain boundary phase. In fact, the Si_{cov} surface coverage was found to be too small (about 0.3 ML) to completely encapsulate the ZrN crystallites. We have also obtained similar results on N-deficient (TaSi)$_y$N$_x$ nanocomposite films [36]. Resistivity Si compositional independent behavior was also reported for nanocomposite TiN/SiN$_x$ films by Jedrzeovski [38].

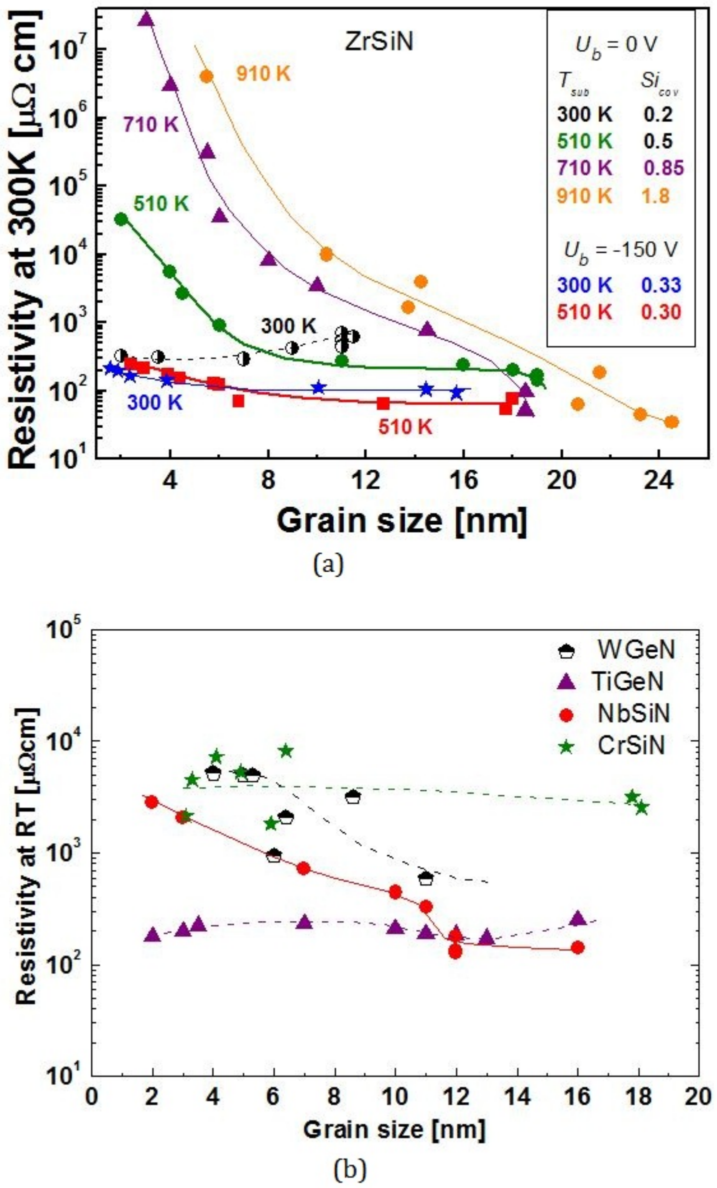

Figure 4. a) Resistivity vs. grain size for Zr-Si-N films deposited at various temperatures and biases. (b) Resistivity vs. grain size for various films.

Furthermore, by comparing the evolution of the resistivity with decreasing grain size for Ti-Ge-N and W-Ge-N composite films, a different behavior is observed (Fig. 4b). This difference gives us information about the electrical nature of the grain boundary phase: conducting $TiGe_x$ phase in the case of Ti-Ge-N films [32] and insulating GeN_x phase in the case of W-Ge-N films [33], which is similar to the insulating SiN_x phase in Nb-Si-N films. In the case of the WC_x-C films, changes in the phase composition from nc-W_2C/nc-WC to nc-WC/a-C are responsible for resistivity variation correlated to the variation of the crystallite size and the presence of high density of point defects [34]. The situation is similar for TiBC films though the presence of three phases, nc-TiB, nc-TiC and a-C, and the large solubility of B in TiC make it difficult the interpretation of results [35]. In WC-C and TiBC nanocomposites, the grain boundary regions composed of a-C do not play a significant role. The main free path of the electrons is mainly limited by the high density of point defects in the amorphous samples whilst lattice defects and grain size predominate in presence of nanocrystalline binary or ternary phases [34,35].

4.1.3. Semiconductor/Insulator (S-I) interfaces

Some MeN such as ScN and CrN are semiconductors. As far as we know, the electrical properties of ScN/SiN$_x$ composites have not been published. In the case of CrN/a-SiN$_x$ system, variation of resistivity with the grain size was also observed [39]. But in the case of a semiconductor material, small variation in the chemical composition of CrN$_x$ crystallites strongly influences the electrical resistivity of the film as shown in Fig. 4b. This could explain the dispersion of the points for the same value of the grain size. This case is the most difficult to model unambiguously. The temperature dependence of the intrinsic resistivity in semiconductor materials masks the temperature dependence of the grain boundary scattering.

4.2. Temperature dependence of d.c. resistivity.

Measuring the electrical resistivity as a function of the temperature gives further information on the main mechanisms responsible of the charge carriers scattering linked to structural changes due to the addition of the second constituent. Fig. 5 shows the temperature dependent d.c. electrical resistivity $\rho(T)$ curves of NbSiN films deposited at 510 K as a function of the Si content [18]. The $\rho(T)$ curves progressively change from metallic-like to non-metallic-like behavior as the Si content in the films increases. These characteristic trends are often observed in (M-I) type of nanocomposites as a function of the concentration of the insulating minority phase. Fig. 6 a and 6b shows few $\rho(T)$ curves of selected nanocomposite films such as ZrSiN, TiGeN, WC-C, and TiBC for specific grain size. In Fig. 6c are presented $\rho(T)$ curves of $Cr_{0.92}Si_{0.08}N_{1.02}$ and CrN_y for $0.93 \leq y \leq 1.15$. Detailed results concerning temperature dependent electrical resistivity can be found in [18] for NbSiN, in [34, 35] for WC-C and TiBC, and in [19] for ZrSiN.

In the case of (M-I) nanocomposites (Fig. 6a), the temperature dependence of resistivity can easily be correlated with film nanostructure (grain size and thickness of the insulating phase). The effect of the electron scattering at grain boundaries is enhanced by the presence of a thin insulating barrier. Thus, the resistivity $\rho(T)$ of Zr-Si-N films with large grain size exhibits metallic behavior (see [19]) while those having small grains exhibit a negative temperature coefficient of resistivity (TCR $=\frac{1}{\rho}\frac{\partial \rho}{\partial T}$). Similar behavior was reported by Piloud in the case of TiBN films [40]. In all these works the authors correlates the negative TCR with the diminution of the crystallite size and the presence of an insulating phase between conducting crystallites.

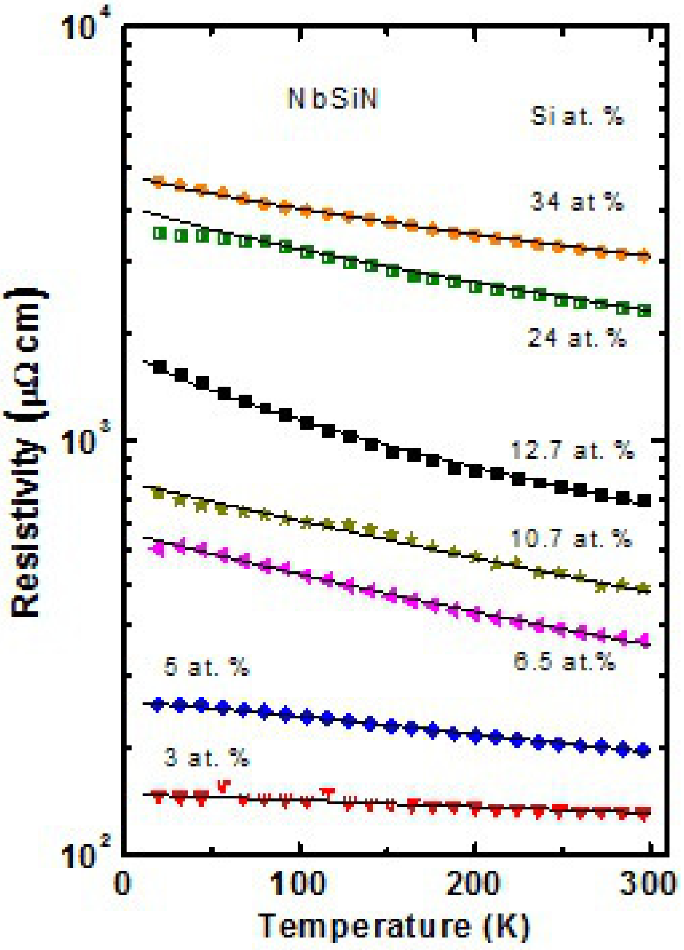

Figure 5. Resistivity vs. Temperature variation for Nb-Si-N films with various Si content.

In the case of (C-C) nanocomposite (TiGeN, WC-C and TiBC), the temperature dependence of resistivity is flat, so the TCR values are low (see Fig. 6b). The resistivity variations for 3 types of films having grain size of about 3nm are similar. The resistivity variation behavior cannot be correlated with the thickness of the phase present at grain boundaries, probably because of a high transmission probability G of charge carriers at the grain boundaries. The absence of the energy gap at GB should be responsible for this.

In the case of (S-I) nanocomposites (CrSiN) the temperature dependence of resistivity (Fig. 6c) cannot easily be correlated with film grain size and scattering probability, because the dependence of polycrystalline semiconducting materials on temperature masks the nanostructure related effects. The change in the N content in CrN_x crystallites significantly influences the resistivity behavior. The resistivity behavior of CrN_x changes from metallic to semiconducting with increasing N content. The formation of a nanocomposite CrN/SiN film with an insulating SiN_x phase between semiconducting CrN crystallites could explain the further increase in resistivity.

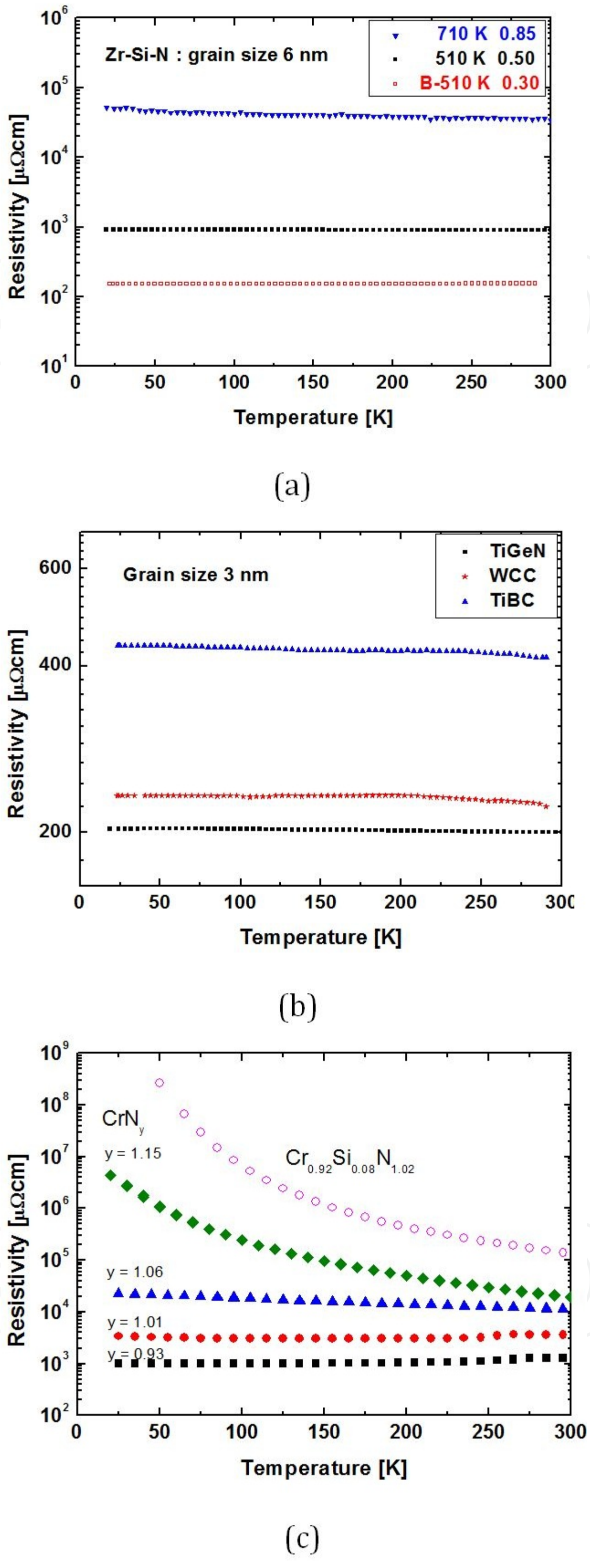

Figure 6. a) Resistivity vs. Temperature variation for Zr-Si-N films with a grain size of 6 nm. (b) Resistivity vs. Temperature variation for various films with a grain size of 3 nm. (c) Resistivity vs. Temperature variation for CrN films with various N/Cr atomic ratios.

5. Grain boundary scattering model

It is frequently observed that the electrical conductivity of thin polycrystalline films strongly deviates from that of the corresponding bulk single-crystalline material. The conductivity is reduced, which commonly is explained by a reduction of the mean free path of electrons (mfp), and often a negative coefficient of resistivity TCR is observed. In the case of quasi-amorphous or heavily distorted materials negative TCR values have been explained by the hopping mechanism or by a week localization of a two-dimensional electron system. However, these models cannot explain all negative TCR values. Based on many experimental results G. Reiss, H. Hoffman *et al*. [41] proposed the grain boundary scattering model for the d.c. resistivity of polycrystalline thin film materials. The authors state that all electrons reflected by the grain boundaries along one mfp do not contribute to the resulting current and the reduction of the conductivity depends exponentially on the number of grain boundaries per mfp. In this model, an effective mean free path $L_G = L\ G^{(L\ /D)}$is introduced to describe the electron scattering at the grain boundaries including the grain size effect; the d.c. electrical conductivity is given by $\sigma = \sigma_B G^{(L\ /D)}$where $\sigma_B$is the bulk conductivity, *G* is the probability for an electron to pass a single grain boundary and *D* is the mean grain size. Under the condition *L/D<<1* the conductivity is reduced to the Drude conductivity without grain boundary effect. The model also predicts a change of the sign of TCR from positive to negative values when *L* and *G* fulfil the condition (*L*/*D*)ln(1/*G*)>2.

Thus, the dc electrical resistivity is then given by

$$\rho_g = \left(\frac{m_e^* v_F}{Ne^2}\right)\left(\frac{1}{L}\right)G^{-(L\ /D)} = \left(\frac{K}{L}\right)G^{-(L\ /D)} \tag{3}$$

where $m_e^*$is the effective masse of the charge carriers, $v_F$is the Fermi velocity, *N* is the density of the charge carriers, *D* is the grain size parameter, *L* is the inner-crystalline mean free path and *G*is the mean probability for electrons to pass a single grain boundary. The inner-crystalline mean free path$L$, describing the volume scattering of electrons, is limited by a temperature invariant elastic scattering at lattice defects and acoustic phonons, namelyl_e, and by the temperature dependent inelastic scattering,l_{in} ,$L^{-1} = l_e^{-1} + l_{in}^{-1}$. The inelastic mean free path is approximated by $l_{in} \approx \alpha T^{-p}$ where α and p are material specific constants.

In nanocomposite materials composed of a main polycrystalline phase (TiN, ZrN, NbN, TaN, CrN, WC, etc) and amorphous minority or tissue phase (SiN_x, GeN, TiB, a-C, etc.) the grain size of the main material, and the thickness and nature of the grain boundary regions can be easily tailored by the volume concentration of the minority phase. The equation (3) gives the possibility, by a simple fitting procedure of $\rho(T)$curves, to obtain pertinent information on the main scattering parameters such as *G*, *D* and l_e. For the theoretical modeling via the relation (3), at the first approximation grain sizes obtained from XRD or HRTEM measurements can be used. Regarding the factor $K = \left(\frac{m_e^* v_F}{N e^2} \right)$, the Fermi velocity and the electron density N are typically in the range of $v_F \approx 1.0\ 10^8$ cm s^{-1} and N= (4-10) 10^{22} cm^{-3}. More precise N values can be obtained from Hall effect or from optical measurements for stoichiometric or defective MeN$_x$ and MeC$_x$. During the fitting procedure, these values can be adjusted to obtain the best fits.

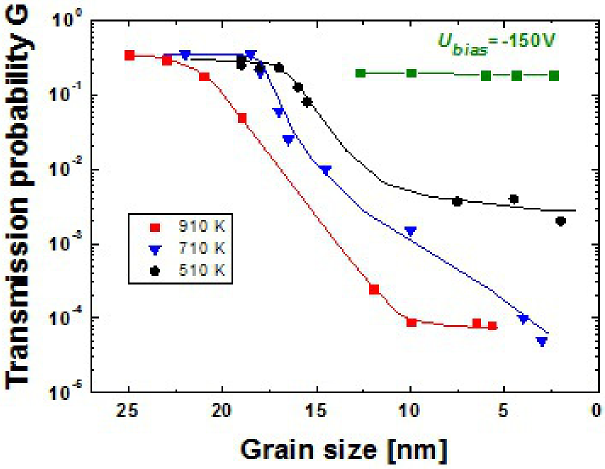

Figure 7. Mean probability G vs. grain size for ZrSiN films deposited at 510, 710 910 K and under bias (lines are added to aid the eye).

The transport mechanisms in nc-NbN/a-SiN$_x$, nc-ZrN/a-SiN$_x$, and nc-TaN/a-SiN$_x$ have been satisfactory described by the grain boundary scattering model. In the case of the Zr-Si-N system, the electrical properties of Zr$_z$Si$_y$N$_x$ films deposited various temperatures, namely, at 300 K (without substrate heating), 510 K, 710 K and 910 K have been investigated in details. It is important to point out that by increasing the substrate temperature the solubility limit of Si, α_L , in the ZrN lattice decreases whereas the Si coverage, Si_{cov}, increases. Thus, the values of the pairs (α_L ,Si_{cov}) are (5 at. %, 0.2), (4 at. %, 0.5), (2 at. %, 0.8) and (1 at. %, 1.8) for the Zr$_z$Si$_y$N$_x$ films deposited at 300 K, 510 K, 710 K and 910 K, respectively. The main probability for electrons to pass the grain boundary G is related to the formation of the SiN$_x$ coverage layer as shown in Fig. 7. In films deposited at 710 K and 910 K, pure ZrN and Zr$_z$Si$_y$N$_x$ films with low Si content (<0.5 at. %) exhibit high G values, G=0.25-0.35. But, for Si content > 1 at%, where the solubility limit is low and the Si coverage important, G deeply decreases down to small values in good correlation with the high thickness values of the SiN$_x$ grain boundary layer (1.6 ML and 3.6 ML, respectively) in these films. For films deposited at 510 K, G decreases slowly and at higher Si content (> 3 at. %) in good agreement with the higher Si solubility and lower thicknesses of the SiN$_x$ layer observed in these films. The electron transmission probability coefficient, G gives us information concerning the continuity and thickness of the insulating phase between conducting grains. In the case of nanocomposites with SiN_x covering layers thinner than 1.0 ML (300 K ZrSiN and 510K ZrSiN with -150 V bias), *G* is larger than 0.05. So, a small scattering probability at grain boundaries implies a small barrier at grain boundaries or the percolation of ZrN crystallites. The effect of the nitrogen content on the electrical nature of the SiN_x grain boundary layer has been investigated in ZrSiN (deposited at 510 K and 710 K with -150 V bias) and in TaSiN films (deposited at 653 K). For N-deficient $(ZrSi)_yN_x$ and $(TaSi)_yN_x$ nanocomposites, the transmission probability *G* remains in the range of 0.1-0.2 over the full investigated Si compositional range(0 – 12 at. %). These results clearly indicate that Si segregation in N-deficient MeSiN films does not lead to the formation of an effective electrically insulating SiN_x layer.

6. SiN_x thickness and resistivity

6.1. Tunneling effect

When two metallic electrodes are separated by an insulating layer (M-I-M structure) the action of the insulating layer is to introduce a potential barrier Φ between the electrodes inhibiting the flow of electrons. However, if the insulating layer is sufficiently thin the current can flow through the insulating region by tunnel effect [42,43]. In the case of electron tunnelling experiments the tunnelling probability is found to be exponentially dependent on the potential barrier width, the tunnelling current is $I_T \propto e^{-\sqrt{\Phi}d} \approx e^{-2.4d}$ and the tunnelling conductance can change by about one order of magnitude for the change $\Delta d \approx 0.1$ nm. Fig. 8 was constructed by considering the thickness of the SiN_x covering layer, as calculated by using the 3-step model for the film formation in the case of ZrSiN films, and the measured resistivity values taken in the region where we have a nanocomposite ZrN/SiN_x structure, as far for the grain size of 4, 6, 8 and 10 nm. The resistivity tends to increases exponentially with the thickness of the SiN_x layer in the range 1.0-3.6 ML (corresponding to a separation distance of 0.2-0.8 nm between metallic crystallites) suggesting that the transport of the electrons across the thin barrier layer seems to occur by tunnelling.

For a M-I-M structure with an insulating layer of thickness *d*, the tunnelling probability T_p for a with a rectangular barrier with an effective barrier height eϕ_B is given by:

$$T_P = exp\left(-2\left[\frac{2m_e^* e\phi_B}{\hbar^2}\right]^{1/2} d\right) \approx exp\left(-\alpha_T\sqrt{\phi_B}d\right) \tag{4}$$

If the effective masse in the insulator is$m_e^* \approx m_e$, the ϕ_B en volts and *d* in Å then α_T=1. The tunnelling conductivity σ_T is given by

$$\sigma_T = \varepsilon_0 \omega_D^2 \tau_T = \left(\frac{Ne^2}{m_e^* v_F}\right) l_e T_P \tag{5}$$

where τ_T is the tunneling relaxation time $\tau_T = \frac{l_e T_P}{v_F}$ and l_e the effective main free path. The tunneling conductivity decreases exponetially with increasing the thickness of the insulating layer. Fig. 9 shows the relationship of the tunneling resistivity and the thickness of the insulating layer with the tunneling probability as calculated from Eq's (4) and (5) for the ZrSiN system. T_P and σ_T have been calculated for two different electron densities N= (1.8-3.6) 10^{22} cm^{-3} for the ZrN, $v_F = 10^8$ cm s^{-1}, l_e=(5-10) nm and for two different effective barrier height values, ϕ_B = 0.6 V and ϕ_B= 1 V. Considering that 1 ML of SiN$_x$ corresponds to about 0.22 nm, the tunneling model predicts that for ϕ_B= 1 V the tunneling probability decreases from 10^{-1} to 10^{-4} and the resistivity increases from about 10^2 μΩ cm up to 10^5 μΩ cm when the thickness of the SiN$_x$ layer change from 1 ML to 4 ML. For lower ϕ_B values, equivalents insulating layers lead to low resistivity values. In Fig. 7 it is shown the transmission probability G, obtained by fitting the ρ(T) experimental curves using the grain boundary scattering model, as a function of the crystallite size (deduced from XRD) for the ZrSiN films deposited at various temperatures. It is worth noting that for films exhibiting comparable crystallite sizes, for instace 12 nm, but with different Si coverages, G values are in the rage of 10^{-1}, 10^{-2} and 10^{-3} corresponding to SiN$_x$ thicknesses of 1ML, 1,6 ML and 3.6 ML, respectively. Though the tunneling conductivity in nanopolycrystallite materials is undoubtedly complexe, the correlation between T_P and G is remarkable. These trends suggest that tunneling conduction should be envolved as one of the the conduction mechanisms responsible for electrons to cross de grain boundary layer between two adjacent crystallites; in particular in the case of elongated crystallites where the length to width ratio higher than 10 have been reported from HRTEM investigations for MeN/SiNx nanocomposites [31,32].

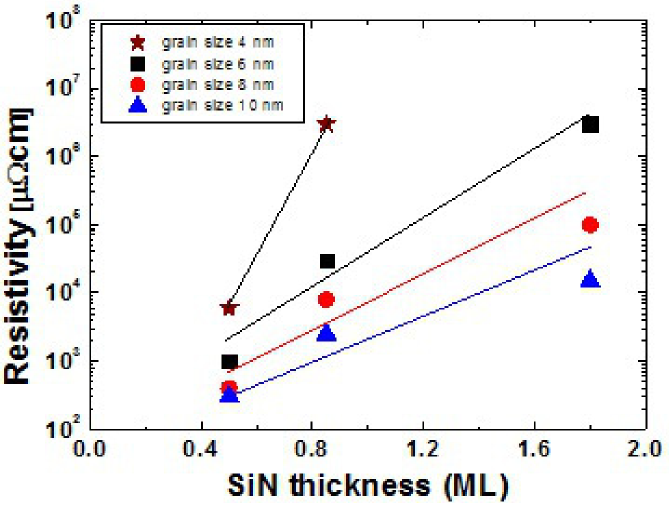

Figure 8. Resistivity vs. thickness of SiN$_x$ interfacial layer: ZrSiN films with 4, 6, 8, and 10 nm crystallite size at 510 K (0.5 ML), 710 K (0.85 ML) and 910 K (1.8 ML). (lines are added to aid the eye).

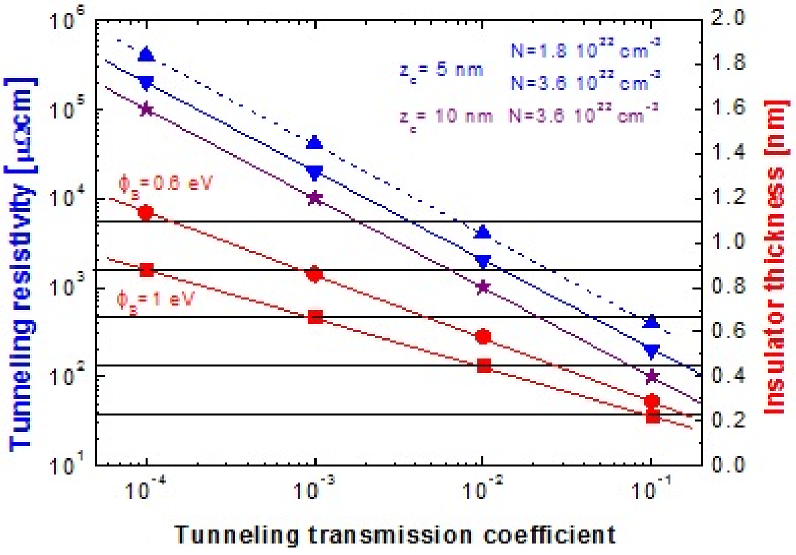

Figure 9. Tunneling resistivity and interfacial insulating thickness vs. tunneling coefficient.

It will be useful to estimate the barrier height eϕ_B in such M-I-M structures. Knowing this value, the transmission probability across metallic-insulating-metallic structures can be calculated as a function of SiN$_x$ thickness. By determining *G* from fitting the resistivity dependence on temperature, we can extract the SiN$_x$ thickness from electrical measurements. We will not speculate that the calculated *G* values are sufficiently precise to then extract the energy gap at the grain boundaries. Rather, we would just like to highlight the good correlation between structural and electrical properties.

6.2. I-V characterisation

To investigate if the observed conductivity in SiN$_x$ thin film results from tunnelling of electrons through the SiN$_x$ thin film current-voltage (I-V) measurements should be performed on Me-SiNx-Me structures. For this purpose, SiN$_x$ films sandwiched between ZrN or TaN have been prepared by magnetron sputtering. These structures have been deposited at 740 K and with bias voltage of -150 V in order to obtain smooth surfaces leading to relatively sharp interfaces. The I-V characteristics for ZrN/SiN$_x$/ZrN structures with different SiN$_x$ thicknesses are show in Fig. 10. The effect of the SiN$_x$ thickness is clearly noticed by comparing the I-V curves with that of the structure without SiN$_x$ layer. For SiN$_x$ thicknesses small than 5 nm (namely the ultrathin regime) the I-V curves show ohmic behaviour, while for thicknesses higher or equal to 5 nm the I-V curves exhibit a symmetric non-linear behaviour. Similar curves have been also observed in the case of TaN/SiNx/TaN structures. The linear behaviour observed in the ultrathin regime can be interpreted in terms of electron tunneling process. A Poole-Frenkel type resistance describes the S-shaped curves, often observed in thin films. In the case of ideal symmetric M-I-M structure the tunnelling current for V< ϕ_B is given by [42]

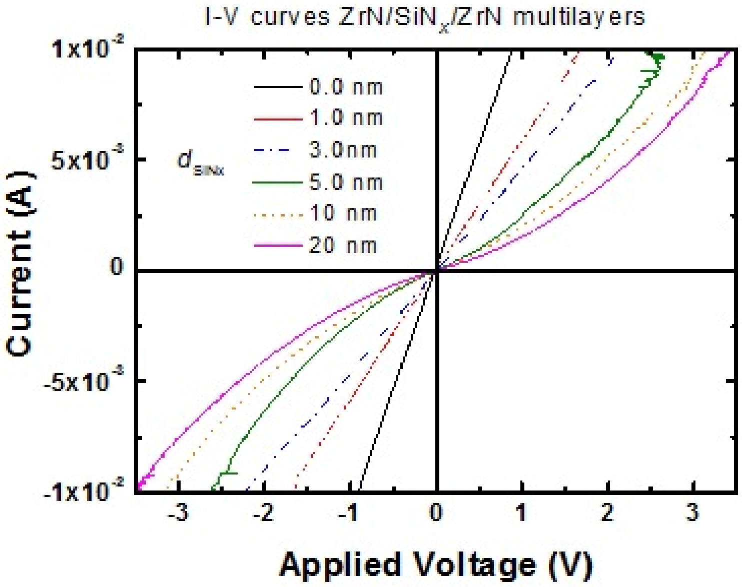

Figure 10. I-V curves in ZrN/SiN/ZrN multilayer films with various insulating SiN layer thicknesses.

$$I = I_0\left[(\phi_B - V/2)exp(-A\sqrt{(\phi_B - V/2)}) - (\phi_B + V/2)exp(-A\sqrt{(\phi_B + V/2)})\right] \tag{6}$$

and for low V range

$$I = \frac{(2m\phi_B)^{1/2}e^2}{2h^2 d} Vexp\left[-2d\sqrt{\frac{2me\phi_B}{\hbar^2}}\right] \tag{7}$$

Earlier studies of the current transport mechanisms in silicon nitride thin films, performed on structures such as Au/Si_3N_4/Mo and Au/Si_3N_4/Si, have shown that the current transport is essentially independent of the substrate material, the film thickness and the polarity of the electrodes [44]. In these studies the Si_3N_4 thickness was in the range of 30 to 300 nm. Depending on the ambient temperature and the electric field three different conduction mechanisms have been identified: Ohmic-type, Poole-Frenkel emission and Fowler-Nordheim tunneling. The Poole-Frenkel mechanism is mainly due to field-assisted excitation from traps and is often observed on defective materials while the Fowler-Nordhein conduction depends on free carriers tunnelling through high quality Si_3N_4 at high electric fields. Ohmic conduction was attributed to the hopping of thermally excited electrons from one isolated state to another.

$$\text{Poole}-\text{Frenkel} \qquad I_{PF} = C_{PF} V exp(-e\phi_B + aV^{1/2} / kT) \tag{8}$$

$$\text{Fowler}-\text{Nordhein} \qquad I_{FN} = C_{FN} V^2 exp(-b / V) \tag{9}$$

$$\text{Ohmic}-\text{type} \qquad I_{Om} = C_{Om} V exp(-e\phi_O / kT) \tag{10}$$

Tao et al [45] have been investigated the effect of N vacancies (Si-Si bonds) and O substitutions (Si-O bonds) on the current-transport properties of $SiN_{1.06}$, $SiN_{1.33}$ and $SiO_{1.67}N_{0.22}$ thin films. The thickness of the Si nitride and of the Si oxynitride layers in Al/SiNO/Si/In structures was typically 15 nm. The results of these studies have been well correlated with the nature of the insulating layer. Thus, all the films exhibit an Ohmic regimen at low electrical fields. The ohmic resistivity depends on the nature of the film; Si-rich films exhibit lower resistivity values while oxynitrides films show the highest values, as the carriers are generated by thermal excitation from traps it was concluded that the density of traps is higher in Si-rich films than in oxynitrides. At intermediate and high electrical fields, Poole-Frenkel emission is the dominant conduction mechanism in Si-rich SiN_x films whereas Fowler-Nordhein tunnelling is mainly involved in oxynitrides films but absent in Si-rich films. Both Poole-Frenkel (at intermediate electrical fields) and Fowler-Nordhein (at high fields) mechanisms are present in nearly stoichiometric Si_3N_4 films.

Based on all these studies we can conclude that the tunnelling current-transport in ultrathin SiN_x layers is very sensitive to N vacancies and to the presence of oxygen atoms. Therefore, Nc-MeN/a-SiN_x nanocomposite thin films containing silicon nitride layers with similar thicknesses but with different chemical composition (sub-stoichiometric or nearly stoichiometric Si_3N_4, oxynitride) can exhibit different electrical properties. Thus, the effects of N-deficiency on the electrical properties of ZrN/SiN_x and TaN/SiN_x nanocomposites as discussed in the section 4 can be interpreted in terms of the presence of high density of free carriers at the grain boundaries thereby leading to high tunnel currents. In addition, the difficulty with real interfaces in thin films is that even if the chemical composition were well controlled surface roughness would increase the local electrical field rising up unexpectedly the tunnel currents.

7. Conclusion

Nanocomposite materials present a high degree of complexity due to small grain size, high curvature radius of nanocrystallites and, in general, a very thin minority phase layer situated at the grain boundaries. Correlating electrical resistivity measurements with film nanostructure provides information concerning the thickness and continuity of the interfacial layer covering conducting nanocrystallites in conducting-insulating nanocomposite films. Aside from some constraints, the possibility to measure experimentally, albeit indirectly, such small interfacial layer thicknesses constitutes an important breakthrough in precise characterization of such nanostructures.

Acknowledgements

The authors wish to thank the Swiss National Science Foundation and the EPFL for financial support.

Author details

R. Sanjinés* and C. S. Sandu

*Address all correspondence to: rosendo.sanjines@epfl.ch

EPFL-SB-ICPM-LPMC, Ecole Polytechnique Fédérale de Lausanne, CH-1015 Lausanne, Switzerland

References

[1] Toth, . E. (1971). *Transition Metal Carbides and Nitrides*, Academic, New York.

[2] Holleck, H., & , J. (1986). *Vac. Sci. Technol. A*, 4, 2661.

[3] Kaloyeros, A. E., & Eisenbraun, E. (2000). *Annu. Rev. Mater. Sci.*, 30, 363.

[4] Riekkinen, T., Molarius, J., Laurila, T., Nurmela, A., Suni, I., & Kivilauhti, J. K. (2002). *Microelectron. Eng.*, 64, 289.

[5] Rossnagel, S. M. (2002). *J. Vac. Sci. Technol.*, B20, 2328.

[6] Wittmer, M. (1980). *Applied Physics Letters*, 36, 456.

[7] Daughton, J. M. (1992). *Thin Solid Films,*, 216, 162.

[8] Sun, X., Kolawa, E., Chen, J., Reid, J. S., & Nicolet, M. A. (1993). *Thin Solid Films*, 236, 347.

[9] Leng, Y. X., et al. (2001). Thin Solid Films, , 398-399.

[10] Wallrapp, F., & Fromherz, P. (2006). *J. Appl. Phys.*, 99, 114103.

[11] Diserens, M., Patscheider, J., & Lévy, F. (1998). *Surf. Coat. Technol.*, 108-109.

[12] Veprek, S., et al. (1999). *J. Vac. Sci. Technol.*, A 17, 2401.

[13] Musil, J. (2000). *Surf. Coat. Technol.*, 125, 322.

[14] Pilloud, D., Pierson, J. F., Marques, A. P., & Cavaleiro, A. (2004). *Surf. Coat. Technol.*, 180-181.

[15] Veprek, S., Maritza, J. G., & Veprek-Heijman, . (2008). *Surf. Coat. Technol.*, 202, 5063.

[16] Sandu, C. S., Sanjinés, R., Benkahoul, M., Medjani, F., & Lévy, F. (2006). *Surf. Coat. Technol.*, 201, 4083.

[17] Martinez, E., Sanjinés, R., Banakh, O., & Lévy, F. (2004). *Thin Solid Films*, 447-448.

[18] Sanjinés, R., Benkahoul, M., Sandu, C. S., Schmid, P. E., & Lévy, F. (2005). *J. Appl. Phys.*, 98, 123511.

[19] Sandu, C. S., Medjani, F., & Sanjinés, R. (2007). *Rev. Adv. Mater. Sci.*, 15-173.

[20] Sandu, C. S., Harada, S., Sanjinés, R., & Cavaleiro, A. (2010). *Surf. Coat. Technol.*, 204, 1907.

[21] Reid, J. S., Kolawa, E., Ruiz, R. P., & Nicolet, M. A. (1993). *Thin Solid Films*, 236, 319.

[22] Kim, D. J., Kim, Y. T., & Park, J. W. (1997). *J. Appl. Phys.,*, 82, 4847.

[23] Lee, Y. J., Suh, B. S., Kwom, M. S., & Park, C. O. (1999). *J. Appl. Phys.*, 85, 1927.

[24] Suh, Y. S., Heuss, G. P., & Misra, V. (2002). *Appl. Phys. Lett.*, 80, 1403.

[25] Letendu, F., Hugon, M. C., Agius, B., Vickridge, I., Berthier, C., & Lameille, J. M. (2006). *Thin Solid Films*, 513, 118.

[26] Olowolafe, J. O., Rau, I., Mr, K., Unruh, C. P., Swann, Z. S., Jawad, T., & Alford, . (2000). *Thin Solid Films*, 365, 19.

[27] Hübner, R., Hecker, M., Mattern, N., Hoffmann, V., Wetzig, K., Heuer, H., Wenzel , Ch , Engelmann, H. J., Gehre, D., & Zschech, E. (2006). *Thin Solid Films*, 500, 259.

[28] Cabral, C., Jr, Saenger, K. L., Kotecki, D. E., & Harper, J. M. E. (2000). *J. Mater. Res.*, 15, 194.

[29] Alén, P., Aaltonen, T., Ritala, M., Leskelä, M., Sajavaara, T., Keinonen, J., Hooker, J. C., & Maes, J. W. (2004). *J. Electrochem. Soc.,*, 151, G523.

[30] Jung, K. M., Jung, M. S., Kim, Y. B., & Choi, K. D. (2009). *Thin Solid Films,*, 517, 3837.

[31] Sandu, C. S., Sanjinés, R., & Medjani, F. (2008). *Surf Coat. Technol*, 202, 2278.

[32] Sandu, C. S., Sanjinés, R., Benkahoul, M., Parlinska-Wojtan, M., Karimi, A., & Lévy, F. (2006). Thin Solid Films ., 496, 336.

[33] Piedade, A. P., Gomes, M. J., Pierson, J. F., & Cavaleiro, A. (2006). Surf. Coat. Technol ., 200, 6303.

[34] Abad, M. D., Sánchez-López, J. C., Cusnir, N., & Sanjinés, R. (2009). *Journal of Applied Physics*, 105, 033510.

[35] Abad, M. D., Sanjinés, R., Endrino, J. L., Gago, R., Andersson, J., & Sánchez-López, J. C. (2011). *Plasma Process and Polymers*, 8, 579.

[36] Oezer, D., Ramirez, G., Rodil, S. E., & Sanjinés, R. submitted to J.A.P

[37] Pierson, J. F., Bertran, F., Bauer, J. P., Jolly, J., & Surf, Ž. (2001). *Coat.Technol.*, 142-144.

[38] Jedrzejowski, P., Baloukas, B., Klemberg-Sapieha, J. E., & Martinu, L. (2004). *J. Vac. Sci. Technol. A*, 22, 725.

[39] Martinez, E., Sanjinés, R., Banakh, O., & Lévy, F. (2004). *Thin Solid Films*, 447-448.

[40] Pilloud, D., Pierson, J. F., & Pichon, L. (2006). *Materials Science and Engineering B*, 131, 36.

[41] Reiss, G., Vancea, J., & Hoffman, H. (1986). *PhysRev.Lett*, 56, 2100.

[42] Simmons, J. G. (1963). *J. Appl. Phys.*,, 34, 1793.

[43] Fisher, J. C., & Giaever, I. (1961). *J. Appl. Phys.*, 32172.

[44] Sze, S. M. (1967). *J. Appl. Phys.*, 38, 2951.

[45] Tao, M., Park, D., Mohammad, S. N., Li, D., Botchkerav, A. E., & Morkoç, H. (1996). *Phil. Mag. B*,, 73, 723.